CHEMISTRY OF MATERIALS

pubs.acs.org/cm

Article

Quantum Effect on the Ground State of the Triple-Perovskite $Ba_3MNb_2O_9$ (M = Co, Ni, and Mn) with Triangular-Lattice

Published as part of the Virtual Special Issue "John Goodenough at 100".

Jinlong Jiao,[+] Shangshun Zhang,[+] Qing Huang, M. Zhang, M.F. Shu, G. T. Lin, C. R. dela Cruz, V. O. Garlea, N. Butch, M. Matsuda, Haidong Zhou,* and Jie Ma*

Cite This: *Chem. Mater.* 2022, 34, 6617−6625

Read Online

ACCESS | Metrics & More | Article Recommendations

ABSTRACT: As the simplest example of geometrical frustration, the two-dimensional triangular lattice antiferromagnet exhibits the mismatch between the lattice geometry and spin-exchange interaction, which has been the subject of intensive studies due to its exotic quantum phenomena. Here, we performed detailed studies of the magnetic structures and spin wave excitations by neutron powder diffraction and inelastic neutron scattering measurements on the triple-perovskite oxides $Ba_3MNb_2O_9$ (M = Co, Ni, and Mn) with triangular-lattice geometry. The interplay between the frustrated interaction and easy-plane/axis anisotropy gives rise to two magnetic phase transition temperatures for $Ba_3CoNb_2O_9$ ($Ba_3MnNb_2O_9$) and only one for $Ba_3NiNb_2O_9$. The linear spin-wave theory $+1/S$ calculations indicate that both spatial dimensionality and the spin size have a significant impact on the strength of quantum fluctuations, which lead to their different magnetic ground states and exotic physical properties. Moreover, the effects of the thermal fluctuations are presented for $Ba_3NiNb_2O_9$.

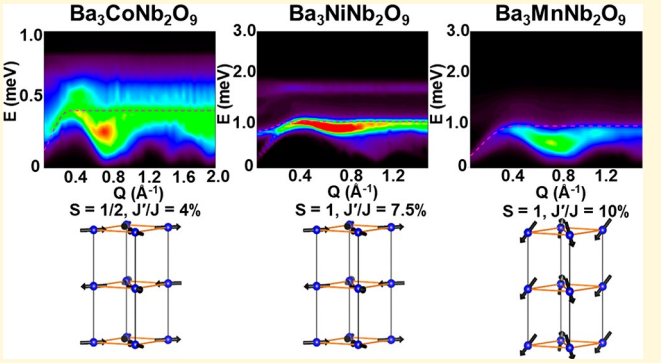

INTRODUCTION

Exploring the exotic quantum phenomena and the related ground states of the quantum magnets has emerged as a forefront area of condensed matter physics,[1−5] and those unconventional states could be created or modified by the delicate relationships among the electron, spin, orbital, and lattice degrees of freedom. One of the intensively investigated materials is the frustrated antiferromagnet with triangular-lattice geometry, which has a large distance between the magnetic layers and exhibits typical two-dimensional (2D) properties with the quantum fluctuation even at the ground state. In 1966, Mermin and Wagner investigated those low-dimensional compounds and found that the long-range magnetic order, breaking a continuous spin-rotation symmetry, can be destroyed by either thermal or quantum fluctuations.[6] However, this continuous symmetry can be broken easily even by a weak interlayer interaction, lattice distortion, and spin or spatial anisotropies, giving rise to the long-range magnetic order below the Néel temperature T_N. For a triangular-lattice antiferromagnet (TLAF), the spins of the ground state arrange in a noncollinear sequency with a coplanar 120° intersection angle between the nearest magnetic ions, which can induce the coupling between transverse and longitudinal fluctuations and cause strong magnon band renormalization and anomalous magnetic excitation continuum featured by a relatively large spectral weight.[7] Therefore, this nonlinear effect intrigues rich physical phenomena and exotic quantum states.

In order to reveal the intrinsic quantum effects of the magnetic ions in the TLAFs, an essential prerequisite is the ideal quasi-2D triangular lattice without lattice distortion or spatial anisotropy. $Ba_3CoSb_2O_9$ is a typical TLAF with an equilateral triangular lattice. Given that the oxygen-octahedron (CoO_6) layers are separated by the double layer nonmagnetic face-shared SbO_6 and Ba^{2+} ions, the interlayer interaction (J') between Co^{2+} ions along the c-axis is much weaker than the intralayer interaction in the ab-plane (J).[8−10] Therefore, it realizes several quantum states, such as the 120° magnetic structure at zero fields and the magnetic field induced "up-up-down" (uud) phase.[8−15] Although $Ba_3CoSb_2O_9$ has been widely studied, the contrast between different TLAF

Received: May 25, 2022
Revised: June 23, 2022
Published: July 5, 2022

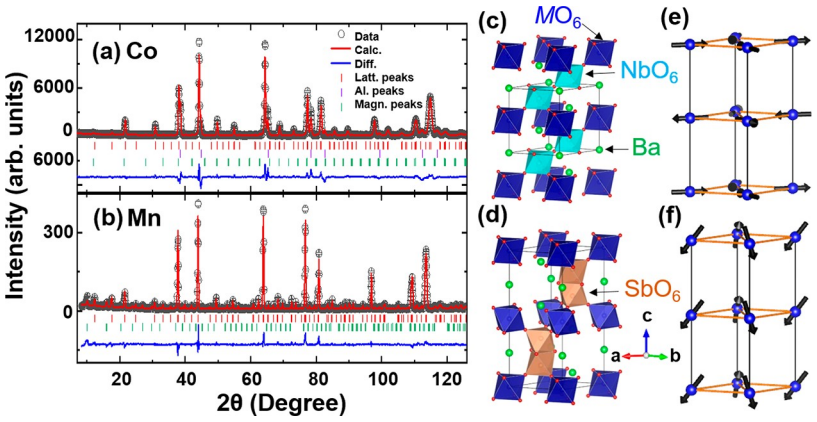

Figure 1. NPD patterns (markers) and Rietveld refinements (red line) using FULLPROF[26] at 244 mK and 1.5 K by HB-2A for (a) $Ba_3CoNb_2O_9$ and (b) $Ba_3MnNb_2O_9$, respectively. Blue lines at the bottom of each panel show the difference between measured and calculated patterns. The red, olive, and purple tick marks are the reflection positions for the lattice phases and magnetic phases of Ba_3MNb_2O9 and the lattice phase of the Al can, respectively. (c,d) Schematic crystal structures for $Ba_3MNb_2O_9$ and $Ba_3CoSb_2O_9$, respectively. (e,f) Schematic magnetic structures for $Ba_3CoNb_2O_9$ ($Ba_3NiNb_2O_9$) and $Ba_3MnNb_2O_9$, respectively.

Table 1. Refined Parameters of $Ba_3MNb_2O_9$ (M = Co, Ni, and Mn) from NPD Results

parameters	$Ba_3CoNb_2O_9$	$Ba_3NiNb_2O_9$[16]	$Ba_3MnNb_2O_9$
space group	$P\bar{3}\ m\ 1$	$P\ \bar{3}\ m\ 1$	$P\bar{3}\ m\ 1$
lattice parameters	$a = b = 5.771(5)$ Å	$a = b = 5.755(2)$ Å	$a = b = 5.804(5)$ Å
	$c = 7.081(7)$ Å	$c = 7.065(6)$ Å	$c = 7.133(4)$ Å
interaxial angles	$\alpha = \beta = 90°$	$\alpha = \beta = 90°$	$\alpha = \beta = 90°$
	$\gamma = 120°$	$\gamma = 120°$	$\gamma = 120°$
k vectors	(1/3 1/3 1/2)	(1/3 1/3 1/2)	(1/3 1/3 0)
moment (μ_B)	1.02(5)	1.81(2)	4.91(2)

Table 2. Selected Bond Lengths (Å), Bond Angles (deg), and Overlap Integral (A) of $Ba_3MNb_2O_9$ (M = Co, Ni, and Mn) at Base Temperature[a]

	$Ba_3CoNb_2O_9$	$Ba_3NiNb_2O_9$[16]	$Ba_3MnNb_2O_9$
in *ab*-plane			
M (A)−M (B)	5.771(5)	5.755(2)	5.804(5)
M (A)−O (1)	2.059(2)	2.053(2)	2.146(2)
O (1)−O (2)	2.862(2)	2.826(2)	2.798(2)
Nb (1)−O	2.013(8)	1.941(3)	1.925(1)
∠Nb(1)−O(1)−O(2)	45.04(3)	45.50(3)	45.56(4)
∠M (A)−O (1)−O (2)	134.96(7)	134.50(7)	134.44(6)
∠M (B)−O (2)−O (1)	134.96(9)	134.51(9)	134.44(7)
∠M (A)−O (1)−Nb (1)	179.10(2)	176.94(5)	176.88(9)
∠O (1)−Nb (1)−O (2)	91.192(3)	93.291(3)	93.244(2)
A	1.155×10^{-4}	1.204×10^{-4}	1.027×10^{-4}

[a]M (A) and M (B) present the A-sublattice and B-sublattice, and O (1) and O (2) are the O^{2-} closest to M (A) and M (B), respectively.

compounds is essential for clarifying the elementary factors that control the strength of quantum effects.

Recently, the theoretical and experimental studies have been extended to $Ba_3MNb_2O_9$ (M = Co, Ni, and Mn),[16−19] a sister family of $Ba_3CoSb_2O_9$. In the Nb-analogue compounds, the Nb^{5+} ion has a larger radius than the Sb^{5+} ion and the NbO_6 octahedra are pushed away from face-sharing to corner-sharing, which not only breaks the glide symmetry along the *c*-axis but also reduces the J'/J by increasing the layer distance between the M^{2+} triangular planes. Hence, the space group changes from $P6_3/mmc$ (no. 194) to $P\bar{3}m1$ (no. 164), and the Nb-analogue compounds keep the regular triangular lattice and avoid the DM interaction.

The spin size (S) is another nonnegligible factor in regulating the quantum effect besides J'.[20−22] For $Ba_3MNb_2O_9$, the combined effect of crystal field and spin−orbit coupling induces a low-energy doublet in the electronic energy configuration of Co^{2+} ($3d^7$) ions, a triplet for Ni^{2+} ($3d^8$) ions, and a sextet for Mn^{2+} ($3d^5$) ions, respectively, which are effectively described by the pseudospin S = 1/2, 1, and 5/2 operators.[23] According to the previous reports,[16−18] $Ba_3NiNb_2O_9$ exhibits only one magnetic transition temperature at T_N = 4.9 K, while $Ba_3CoNb_2O_9$ and $Ba_3MnNb_2O_9$ have two at 1.36, 1.10, and 3.4 K, 3.0 K, respectively. It is obvious that although $Ba_3MnNb_2O_9$ has the largest spin size, S = 5/2, $Ba_3NiNb_2O_9$ has the highest magnetic transition temperature.

This paper conducted the first systematic study on the spin dynamic spectra of the triple-perovskite $Ba_3MNb_2O_9$. The reduction of the quantum fluctuation by the interlayer interaction, exchange or single-ion magnetic anisotropy, and

https://doi.org/10.1021/acs.chemmater.2c01576
Chem. Mater. 2022, 34, 6617−6625

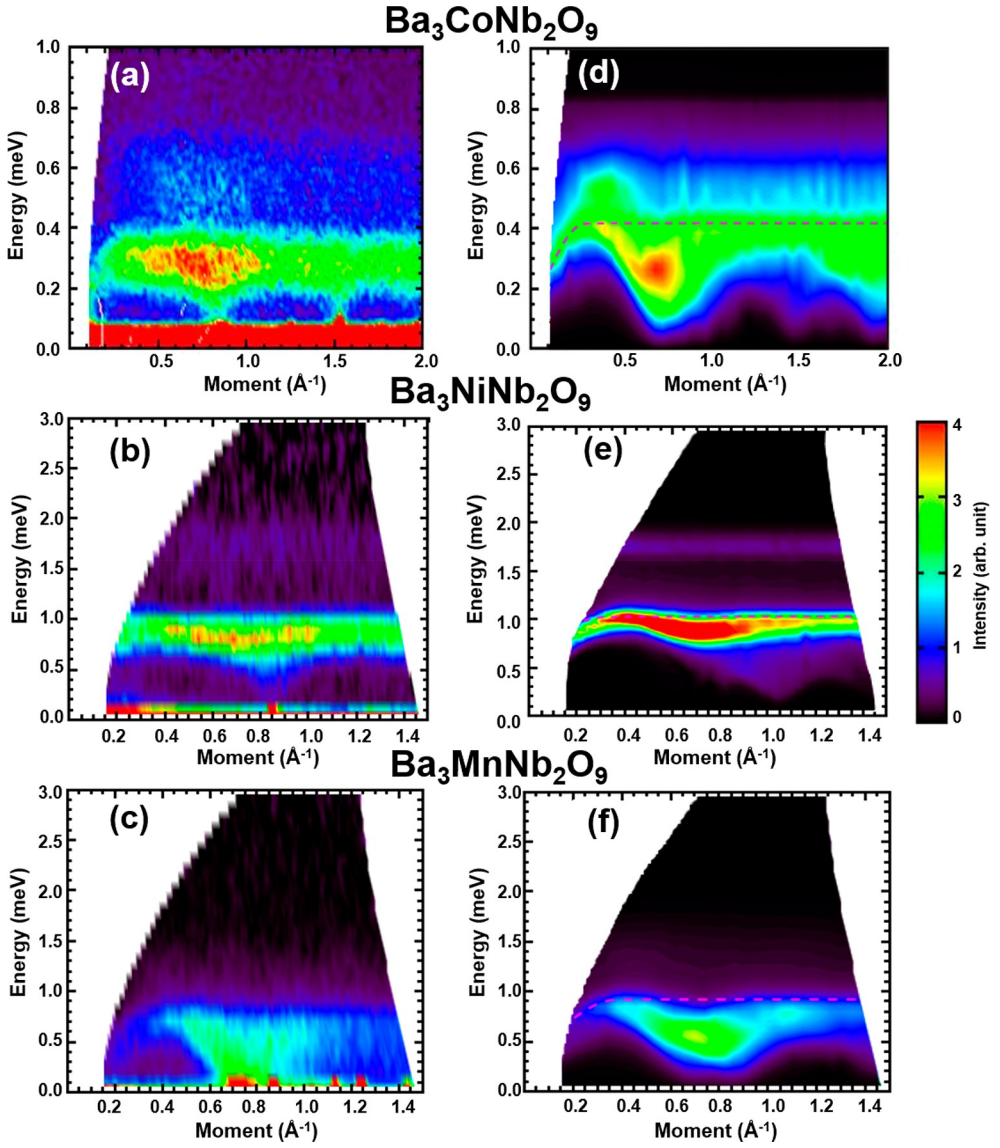

Figure 2. Experimental spectra of energy versus momentum transfer for (a) $Ba_3CoNb_2O_9$ with E_i = 3.27 meV at 0.2 K, (b) $Ba_3NiNb_2O_9$, and (c) $Ba_3MnNb_2O_9$ with E_i = 3.8 meV at 1.5 K, respectively. (d–f) The calculated powder averaged dynamical spin structure factor using spin wave theory by LSWT + 1/S corrections.

the spin size are studied quantitatively based on a modified Heisenberg TLAF model that is compatible with both space group symmetry and the ground-state magnetic ordering. The origins of the exchange interactions are discussed quantitatively according to the underlying microscopic lattice structure. This generic understanding built from the reduction of the quantum effects applies to other frustrated magnets.[24,25]

RESULTS AND DISCUSSION

Neutron Powder Diffraction (NPD). The NPD patterns of $Ba_3CoNb_2O_9$ and $Ba_3MnNb_2O_9$ at 244 mK and 1.5 K are presented in Figure 1a,b, respectively. The diffraction patterns of $Ba_3CoNb_2O_9$ and $Ba_3NiNb_2O_9$ are similar,[16,17] which is not shown here, while $Ba_3MnNb_2O_9$ shows more Bragg peaks than theirs. There are no impurity peaks observed and the antisite disorder between the magnetic M^{2+} and nonmagnetic Nb^{5+} ions is neglectable. The refined lattice parameters and selected bond lengths and angles are listed in Tables 1 and 2, respectively. Figure 1c presents the schematic crystal structures for $Ba_3MNb_2O_9$. The M^{2+}, Ba^{2+}, Nb^{5+}, and O^{2-} ions are sequentially distributed in the alternating layers stacked along the c-axis. The M^{2+} and Nb^{5+} ions are at the center of an octahedron surrounded by six O^{2-} ions, and NbO_6 and MO_6 octahedra are connected by the O^{2-} ion at the vertices. Meanwhile, the M^{2+} ions form a perfect equilateral triangular lattice without distortion. The crystal structure of $Ba_3CoSb_2O_9$ is demonstrated in Figure 1d for comparison, in which the SbO_6 octahedra share the O^{2-}-face instead. As a consequence, the exchange path of the magnetic ions in different layers is different between $Ba_3CoNb_2O_9$ and $Ba_3CoSb_2O_9$, as discussed below. It is noticed that the M–M bond lengths of $Ba_3NiNb_2O_9$ are shortest both in the ab-plane and along the c-axis, which can be explained by the smallest ion radius of the Ni^{2+} ion (0.690 Å) compared with other M^{2+} ions (M = Co, 0.745 Å; Mn, 0.830 Å for the high-spin state).[27]

Although all three oxides are isostructural, the magnetic propagation vectors are (1/3, 1/3, 1/2) for $Ba_3CoNb_2O_9$ ($Ba_3NiNb_2O_9$) and (1/3, 1/3, 0) for $Ba_3MnNb_2O_9$,

https://doi.org/10.1021/acs.chemmater.2c01576
Chem. Mater. 2022, 34, 6617–6625

respectively. The ordered moments for these three oxides from refinements are 1.02 μ_B, 1.81 μ_B, and 4.91 μ_B, respectively, which agree with the reported results and can be described as pseudospin 1/2, 1, and 5/2 spin states.[16−18] The magnetic structures for all three compounds in the magnetic triangular-layer (*ab*-plane) are the 120° spin structure, while they are different along the *c*-axis. As shown in Figure 1e,f, the spins of $Ba_3CoNb_2O_9$ ($Ba_3NiNb_2O_9$) lie in the *ab*-plane and are antiferromagnetic (AFM) along the *c*-axis, while the spins of $Ba_3MnNb_2O_9$ are parallel with a small canting angle along the *c*-axis corresponding to an easy-axis type (the spins on two sublattices are 8.7° downward from the *ab*-plane and the other sublattice are 18.7° upward from the *ab*-plane).

Inelastic Neutron Scattering and Simulation. To study the quantum effect on the spin dynamics, the inelastic neutron scattering (INS) measurements were performed. Figure 2a−c show the energy-momentum maps of the scattering intensity of $Ba_3MNb_2O_9$. The scattering data was collected at 0.2 K with incident neutron energy E_i = 3.27 meV for $Ba_3CoNb_2O_9$, Figure 2a, and 1.5 K with E_i = 3.8 meV for $Ba_3NiNb_2O_9$ and $Ba_3MnNb_2O_9$, Figure 2b,c, respectively. All measuring temperatures were below T_N.[16−18] The spin dynamic spectra of $Ba_3MNb_2O_9$ all show minima around $Q \approx 0.7$ Å^{-1}, which corresponds to the commensurate magnetic ordering wavevector (1/3, 1/3, 1/2) for $Ba_3CoNb_2O_9$ ($Ba_3NiNb_2O_9$) and (1/3, 1/3, 0) for $Ba_3MnNb_2O_9$. For the Co-compound (Figure 2a), the scattering intensities at $Q \approx 0.7$ Å^{-1} are stronger than at $Q \approx 1.5$ Å^{-1} and $Q \approx 2.0$ Å^{-1}, manifesting the momentum-dependence of magnetic signals. The spectrum has two separated energy bands. The lower energy part originates from the single-magnon excitations with a bandwidth of about 0.4 meV. The quasi-gapless feature at $Q \approx 0.7$ Å^{-1} indicates an approximately SU(2) spin-rotation symmetry. The higher energy band compromises a continuum of magnetic excitations extending up to 0.8 meV. The Ni-compound has a similar spectral structure (Figure 2b), except (i) a less dispersive and gapped low-energy band, (ii) a weaker intensity from the high energy band centered at 1.8 meV, and (iii) a wider separation between the low- and high-energy bands. These observations imply a more significant magnetic anisotropy in the model Hamiltonian for the Ni-compound. It also partly explains why the Ni-compound has the highest magnetic transition temperature among this family. For the Mn-compound, Figure 2c, we observed one gapped and dispersive mode at low energy, while the high-energy band observed for the other two compounds is invisible here. This typical semiclassical behavior indicates relatively weak quantum fluctuations in $Ba_3MnNb_2O_9$ compared to the other two compounds. By comparing the powder-averaged magnetic dynamics of these three compounds, we clearly observed that the strength of the quantum effect decreased with increasing spin size (S).

We simulated the INS spectra by the linear spin wave theory (LSWT) based on a modified spin-exchange Hamiltonian compatible with both space group symmetry and the ground state magnetic ordering of $Ba_3MNb_2O_9$, Figure 2d−f. For M = Co or Ni, the spins form the coplanar 120° order within the *ab*-plane and align antiferromagnetically along the *c*-axis. This magnetic structure can be explained by the quasi-2D XXZ Hamiltonian including both spin-exchanges on the nearest neighbor (NN) bonds in the *ab*-plane and that on the vertical bonds along the *c*-axis,

$$H_1 = J \sum_{<ij>\perp c} (S_i^x S_j^x + S_i^y S_j^y + \Delta S_i^z S_j^z) + J' \sum_{<ij>\| c} S_i \cdot S_j \quad (1)$$

where $J > 0$ and $J' > 0$ are the antiferromagnetic intra- and interlayer NN spin-exchange energies, and $0 < \Delta < 1$ is the easy-plane spin-exchange anisotropy.

For M = Mn, the ground state develops a noncoplanar magnetic structure as discussed above. The layers stack ferromagnetically along the *c*-axis, indicating that the interlayer coupling is $J' < 0$ ferromagnetic. To explain this noncoplanar magnetic structure, a generic spin-exchange Hamiltonian that includes all symmetry-allowed terms is not enough. The essential term is the single-ion anisotropy, which takes the following generic form for spin-5/2 magnetic Mn^{2+} ions,

$$H_D = D_1 \sum_i (S_i^z)^2 + D_2 \sum_i (S_i^z)^4 + D_3 \sum_i (S_i^z)^6 \quad (2)$$

where D_1, D_2, and D_3 are independent to the magnetic sublattices. We note that the minimal model, $H_1 + H_D$, must include nonzero D_1 and D_2, as we did in the calculation. The easy-plane spin-exchange anisotropy is expected to be small (Δ*is* close to 1) given the quasi-gapless nature of the INS spectra shown in Figure 2(c).

The simulated spectra shown in Figure 2d−f agree well with the experimental INS spectra, while Table 3 lists the model parameters adopted in the LSWT calculations. The pink dashed line in the simulated spectra separates the single-magnon and the two-magnon excitations, which corresponds to the low- and high-energy bands in the INS spectra, respectively. The spectral weight associated with the two-magnon continuum comes from the $1/S$ correction to the LSWT calculation and measures the magnitude of quantum fluctuations. From both experimental data and the calculation, the weight of the two-magnon continuum is the largest for $Ba_3CoNb_2O_9$ ($S(Co^{2+}) = 1/2$), strongly suppressed for $Ba_3NiNb_2O_9$ ($S(Ni^{2+}) = 1$), and almost negligible for $Ba_3MnNb_2O_9$ ($S(Mn^{2+}) = 5/2$), which confirms that $Ba_3CoNb_2O_9$ has the strongest quantum fluctuations in the $Ba_3MNb_2O_9$ (M = Co, Ni, and Mn) system. Actually, such quantum-effect related continuum mode had been observed in other frustrated systems, such as $Ba_3CoSb_2O_9$,[8,11] $NaYbCh_2$ (Ch = chalcogenide),[28−31] $Na_2Co_2TeO_6$,[32,33] etc. The bandwidth of the single-magnon excitations is larger in the calculation compared with the data. It further reduces through the interaction with the two-magnon continuum as described by the cubic term in the spin-wave Hamiltonian.[7,34]

To determine the thermal fluctuation on the quantum effect, the temperature dependence of the INS spectra of $Ba_3NiNb_2O_9$ was measured. As shown in Figure 3, the

Table 3. Summary of Parameters in the Hamiltonian of the LSWT Results

parameters	$Ba_3CoNb_2O_9$	$Ba_3NiNb_2O_9$	$Ba_3MnNb_2O_9$	$Ba_3CoSb_2O_9$[8]
J (meV)	0.25	0.32	0.1	1.7
J' (meV)	0.01	0.015	−0.01	0.085
$\|J'\|/\|J\|$	4%	7.5%	10%	5%
Δ	0.996	0.625	0.99	0.94
D_1 (meV)			−0.004	
D_2 (meV)			0.003	
D_3 (meV)			0	

https://doi.org/10.1021/acs.chemmater.2c01576
Chem. Mater. 2022, 34, 6617−6625

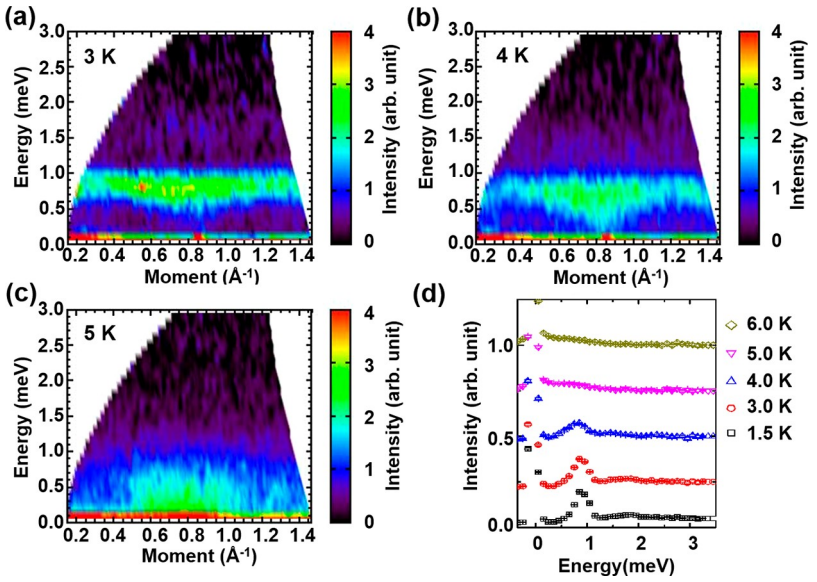

Figure 3. Temperature dependence of inelastic neutron scattering intensity of $Ba_3NiNb_2O_9$ versus energy and momentum transfer by HYSPEC, SNS. (a–c) The INS spectra of $Ba_3NiNb_2O_9$ measured at 3, 4, and 5 K, respectively. (d) Temperature dependence of the momentum-integrated ($0.2 \leq Q \leq 1.2$ Å $^{-1}$) intensity.

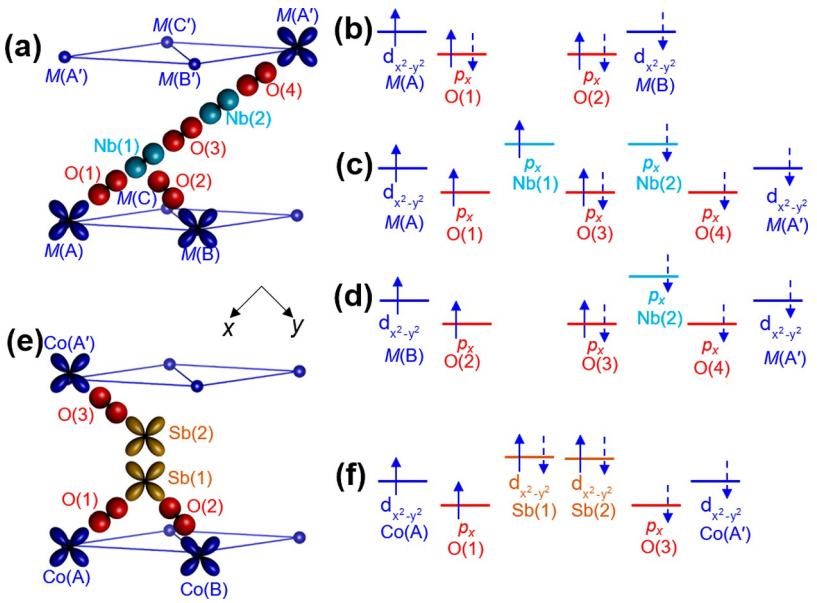

Figure 4. (a) The SSE interaction paths for $Ba_3MNb_2O_9$, here, only the $d_{x^2-y^2}$ orbitals of magnetic ions were considered. The index M (A)–M (C) and M (A′)–M (C′) present different sublattices. For the Nb-analogue compounds, the intralayer NN exchange interaction is achieved via (b) $d_{x^2-y^2}$(M(A))–p_x(O(1))–p_y(O(2))–$d_{x^2-y^2}$(M(B)) and the interlayer NN exchange interaction is accompanied via (c) $d_{x^2-y^2}$(M(A))–p_x(O(1))–p_x(Nb(1))–p_x(O(3))–p_x(Nb(2))–p_x(O(4))–$d_{x^2-y^2}$(M(A′))for M (A)–M (A′), and (d) $d_{x^2-y^2}$(M(B))–p_x(O(2))–p_x(O(3))–p_x(Nb(2))–p_x(O(4))–$d_{x^2-y^2}$(M(A′)) for M (B)–M (A′). (e) The SSE interaction paths for $Ba_3CoSb_2O_9$; here, only the $d_{x^2-y^2}$ orbitals of magnetic ions were considered. (f) The interlayer NN exchange interaction path for $Ba_3CoSb_2O_9$, which is accompanied via $d_{x^2-y^2}$(Co(A))–p_x(O(1))–$d_{x^2-y^2}$(Sb(1))–$d_{x^2-y^2}$(Sb(2))–p_y(O(3))–$d_{x^2-y^2}$(Co(A′)). The solid and dotted arrows in parts b–d, and f present the spin directions of the two interacting magnetic ions, respectively.

integrated magnetic scattering versus energy was integrated from ~0.2 Å^{-1} to ~1.2 Å^{-1}. With increasing temperature, the scattering intensities of the two distinct magnetic excitation modes both decrease, and the energies of both bands demonstrate different behaviors: the energy of the low energy magnon band is kept constant, while the high energy continuum band moves toward the lower energy side (Figure 3d). Above T_N (~5 K), the higher energy band disappears while the low energy magnon band turns into a diffused paramagnetic dynamics from the AFM ordering. Hence, the quantum effect related continuum mode can be modulated by temperature easily.

The three compounds are distinctive in magnetic anisotropy. $Ba_3CoNb_2O_9$ shows a nearly isotropic feature with $\Delta = 1$, $Ba_3NiNb_2O_9$ has a large easy-plane spin-exchange anisotropy with $\Delta = 0.625$, and $Ba_3MnNb_2O_9$ presents a small easy-axis single-ion anisotropy in eq 2 with nonzero D_1 and D_2. As theoretically predicted in the triangular system,[35−39] these

https://doi.org/10.1021/acs.chemmater.2c01576
Chem. Mater. 2022, 34, 6617−6625

distinct anisotropies are responsible for different finite temperature phase transitions. A relatively large easy-plane spin-exchange anisotropy stabilizes the 120° order within the easy plane. It melts at the Néel temperature through a single transition to a paramagnet. By contrast, the interplay between a weak easy-plane anisotropy and an easy-axis, single-ion anisotropy induces a two-step transition,[40] giving rise to the low-T 120° order, the intermediate-T up-up-down order, and the high-T paramagnet. The above two scenarios are consistent with our measurements of $Ba_3NiNb_2O_9$ and $Ba_3MnNb_2O_9$, respectively. For a (nearly) isotropic system with $S = 1/2$, advanced numerical studies indicate two temperature scales related to the developments of antiferromagnetic and scalar chiral correlations.[39] While this provides one possible scenario for the two-step transition observed in $Ba_3CoNb_2O_9$, its exact nature remains elusive, given the presence of spontaneous ferroelectricity in this material.[18] How the magnetic orderings intertwine with the ferroelectricity calls for future studies.

As the Hamiltonian for the three compounds has the U(1) spin-rotation symmetry about the c-axis, the low-energy excitations should contain a gapless Goldstone mode at the Brillouin zone (BZ) center. Meanwhile, the absence of the SU(2) symmetry due to the easy-plane spin-exchange anisotropy and the single-ion anisotropy induces a spin gap at the BZ boundary. As revealed in the experimental spectra, the strongest anisotropy for $Ba_3NiNb_2O_9$ leads to a much flatter band, while the small anisotropy for $Ba_3MnNb_2O_9$ causes a small spectral gap.

Exchange Paths and Exchange Energy. Besides the spin-moment effect, the exchange energies of both the intralayer J and interlayer J' affect the quantum effect of the triangular system. There are two supersuper exchange (SSE) interaction paths for the NN ions in the ab plane, as shown in Figure 4a. The first SSE path of M (A)−O (1)−O (2)−M (B) is realized along the two bridging NbO_6 octahedra and does not include the Nb^{5+} ion, and the other path is along M (A)−O (1)−Nb (1)−O (2)−M (B) with two nearly 180° angles (M (A)−O (1)−Nb (1) and M (B)−O (2)−Nb (1)). As illustrated in refs 19 and 41, the second path presents a weak ferromagnetic (FM) SSE through the extra Nb^{5+} ion; hence, only exchange energy via the first path was considered in this article. By following the analysis method in ref 42, the exchange interactions between the electrons on the t_{2g} and e_g orbitals were discussed microscopically for $Ba_3MNb_2O_9$ using the angle and bond lengths listed in Table 2, respectively.

For the SSE path of (M (A)−O (1)−O (2)−M (B)) in the ab-plane, Figure 4b, the NN magnetic M^{2+} ions interact with each other via two bridging oxygen 2p orbitals. Assuming the interaction of M^{2+} ions is through the $d_{x^2-y^2}$ (e_g) orbitals, the spins of the left M^{2+} ion (M(A)) and right M^{2+} ion (M (B)) achieve the interaction first by forming a σ-type bond with the bridged oxygen p_x and p_y orbitals, respectively. Thereafter, the two spins would interact further on a concrete 2p orbital (p_x or p_y) to finish the exchange by the overlap of p_x and p_y orbitals. The AFM nature is decided by the Goodenough−Kanamori law, and the exchange coupling was governed by the Pauli principle on the O 2p orbital. As the distorted triangular oxides $A_3NiNb_2O_9$ (A = Ca, Sr)[19] and the dimer oxide $Ba_3LaRu_2O_9$,[43] the AFM interaction is strong through the super-super exchange. Actually, the interaction between M^{2+}(A) and M^{2+}(B) ion is valid not only for the e_g−e_g electrons but also works for t_{2g}−t_{2g} and t_{2g}−e_g electrons. The only prohibited path of the hopping p_x and p_y orbitals is that both bond angles of the ∠M (A)−O (1)−O (2) (θ_1) and ∠M (B)−O (2)−O (1) (θ_2) are 90°. Therefore, the strength of this SSE is associated with the degree of deviation from 90° for θ_1 and θ_2 angles. Since the exchange constant J is decided by $4t^2/U$, where U is the on-site Coulomb repulsion and t is the orbital overlap integral that depends on the bond length of two neighbor atoms, the strength of this AFM interaction could be quantitated by both the bond angles and bond lengths. For the superexchange interaction pathways involved in perovskite-structured oxides,[44] the orbital overlap integral was proportional to the factor $\sqrt{A} = \cos^2(\omega/2)/d^{3.5}$. The exchange energy in the triple-perovskite system then is obtained by the average-effect: d is the average bond length of M (A)−O (1), O (1)−O (2), and O (2)−M (B), and ω is the angle consisting of ∠Nb (1)−O (1)−O (2). The bond lengths and bond angles were obtained from the NPD refinements, and the factor As for these three materials were calculated and summarized in Table 2. Compared with $Ba_3CoNb_2O_9$ and $Ba_3MnNb_2O_9$, $Ba_3NiNb_2O_9$ has the biggest A, which determines its strongest AFM interaction.

As illustrated in Figure 4c, the magnetic ion M (A) on the first layer triangular lattice accomplishes the exchange interaction with the diagonal M (A′) on the second layer triangular lattice via the SSE interaction path of $d_{x^2-y^2}$(M(A))−p_x(O(1))−p_x(Nb(1))−p_x(O(3))−p_x(Nb(2))−p_x(O(4))−$d_{x^2-y^2}$(M(A′)). The spins from M (A) and M (A′) are correlated by the p_x orbital of the middle O^{2-}. Then, they would arrange antiparallelly and transfer back to M^{2+} by the Pauli principle. It is noteworthy that the hole from M (A′) could also interact with that from M (B) through $d_{x^2-y^2}$(M(B))−p_x(O(2))−p_x(O(3))−p_x(Nb(2))−p_x(O(4))−$d_{x^2-y^2}$(M(A′)) to produce AFM interaction, as shown in Figure 4d. Consequently, the AFM exchange interaction among M (A)−M (B), M (A)−M (A′), and M (B)−M (A′) compete with each other and lead to the frustration of the interlayer exchange interaction. Therefore, whether J' could be FM or AFM would depend on the result of this competition. For $Ba_3MNb_2O_9$, $Ba_3CoNb_2O_9$, and $Ba_3NiNb_2O_9$ exhibit AFM J' while $Ba_3MnNb_2O_9$ presents FM J'. In fact, this qualitative discussion on the exchange energy could be applied for other compounds: for $Na_2BaMV_2O_8$ (M = Co, Ni, and Mn),[45] $Na_2BaMnV_2O_8$ presents AFM ordering while $Na_2BaCoV_2O_8$ and $Na_2BaNiV_2O_8$ present FM ordering; for $Ba_2La_2MW_2O_{12}$ (M = Co, Ni, and Mn),[46] $Ba_2La_2MnW_2O_{12}$ shows FM ordering while both $Ba_2La_2CoW_2O_{12}$ and $Ba_2La_2NiW_2O_{12}$ exhibit AFM ordering.

For the NbO_6 corner-shared $Ba_3CoNb_2O_9$, the sum bond length through the path in the ab-plane (Co (A)−O (1)−O (2)−Co (B)) is L = 6.97 Å, and the sum bond length through the path along the c-axis (Co (A)−O (1)−Nb (1)−O (3)−Nb (2)−O (4)−Co (A′)) is L' = 12.25 Å. Hence, L'/L ($Ba_3CoNb_2O_9$) is 1.757. For the SbO_6 face-shared $Ba_3CoSb_2O_9$, Co (A)-ion in the bottom layer could achieve AFM exchange interaction with the Co (A′)-ion in the top layer, which is right above the Co (A)-ion via $d_{x^2-y^2}$(Co(A))−p_x(O(1))−$d_{x^2-y^2}$(Sb(1))−$d_{x^2-y^2}$(Sb(2))−p_y(O(3))−$d_{x^2-y^2}$(Co(A′)), Figure 4e,f. From the crystal information in ref 8, L and L' for $Ba_3CoSb_2O_9$ are 7.102 and 10.908 Å, respectively. Then, $\frac{L'/L(Ba_3CoSb_2O_9)}{L'/L(Ba_3CoNb_2O_9)} = 87\%$ is deduced, which is very close to the $\frac{J'/J(Ba_3CoNb_2O_9)}{J'/J(Ba_3CoSb_2O_9)} = 80\%$. Therefore, replacing the intersecting SbO_6 octahedra by NbO_6 octahedra could

https://doi.org/10.1021/acs.chemmater.2c01576
Chem. Mater. 2022, 34, 6617−6625

decrease the interlayer exchange interaction and makes $Ba_3CoNb_2O_9$ more 2D-like.

Furthermore, J'/J is 7.5% for $Ba_3NiNb_2O_9$, which is due to the shorter bond length compared with $Ba_3CoNb_2O_9$. Also, it is no doubt that this reduced space distance between the layers weakens the quantum effect. For $Ba_3MnNb_2O_9$, the biggest J'/J = 10% arises from its largest resultant ferromagnetic exchange interaction although it doesn't have the shortest bond length. The biggest value of spin is the reason why it does not show quantum effect.

CONCLUSION

In conclusion, we regulated the quantum fluctuations of TLAFs at the momentum- and space-dimension and found that the quantum effect gradually weakens from a smaller spin (S = 1/2) to a larger spin (S = 5/2). The triple-perovskite oxides $Ba_3MNb_2O_9$ (M = Co, Ni, and Mn) are different in magnetic anisotropy: $Ba_3CoNb_2O_9$ exhibits isotropic behavior, $Ba_3NiNb_2O_9$ has easy-plane exchange anisotropy, and $Ba_3MnNb_2O_9$ presents easy-axis single-ion anisotropy. The distinct anisotropy not only determines different numbers of macroscopic phase transition temperatures but also induces different spin-dynamic spectra. $Ba_3NiNb_2O_9$ only has one transition temperature, while $Ba_3CoNb_2O_9$ and $Ba_3MnNb_2O_9$ have two. The different bond lengths and bond angles of the SSE paths determine the exchange energy of $Ba_3MNb_2O_9$, while the origin of the exchange energy is compared in both $Ba_3CoNb_2O_9$ and $Ba_3CoSb_2O_9$. $Ba_3NiNb_2O_9$ has the shortest bond length, which determines its maximum exchange energy and maximum phase transition temperature. Furthermore, the thermal fluctuation on the quantum effect in $Ba_3NiNb_2O_9$ was observed.

METHODS

Sample Preparation and Characterization. Polycrystalline samples of $Ba_3MNb_2O_9$ (M = Co, Ni, and Mn) were prepared by the solid-state reaction method. Stoichiometric mixtures of $BaCO_3$, Co_3O_4/NiO/MnO, and Nb_2O_5 were ground together and calcined in air at 1230 °C for 24 h. Also, the compounds were characterized by the bulk measurements, which have been reported previously.[16−18]

Neutron Diffraction and Inelastic Neutron Scattering. The neutron powder diffraction (NPD) data were obtained by using the HB-2A powder diffractometer at the High Flux Isotope Reactor (HFIR), the Oak Ridge National Laboratory (ORNL). About 5 g of powder for each composition was loaded in a vanadium can with an inner diameter of 12 mm. To obtain the structure of the ground state, $Ba_3CoNb_2O_9$, $Ba_3NiNb_2O_9$, and $Ba_3MnNb_2O_9$ were measured at 244 mK, 2 K, and 1.5 K, respectively. Two different wavelengths were applied with λ = 1.538 and 2.406 Å and the collimation is 12′-open-6′. The shorter wavelength gives a higher Q coverage and was used to investigate the crystal structures, while the longer wavelength gives lower Q coverage and was used investigate the magnetic structures of the material. The diffraction data were refined by the Rietveld method using FULLPROF.[26]

The inelastic neutron scattering (INS) measurements were performed on the Hybrid Spectrometer (HYSPEC) for $Ba_3NiNb_2O_9$ and $Ba_3MnNb_2O_9$ at the Spallation Neutron Source (SNS), ORNL, and the Disk Chopper Spectrometer (DCS) for $Ba_3CoNb_2O_9$, NIST Center for Neutron Research (NCNR), respectively. Both instruments are direct geometry time-of-flight (TOF) spectrometers and applied for measuring the scattering intensity, $S(Q, \omega)$, over a wide range of scattering energy transfers, ω, and momentum transfers, Q. About 4 g of powder for each composition was loaded in an aluminum can filled with He exchange gas and were measured at 244 mK for $Ba_3CoNb_2O_9$ and 1.5 K for $Ba_3NiNb_2O_9$ and $Ba_3MnNb_2O_9$. Each scan was counted around 6 h with the incident neutron energies λ_i = 1.436 and 5.595 Å at HYSPEC and λ_i = 1.8 and 5 Å at DCS. The INS data were analyzed by DAVE.[47]

AUTHOR INFORMATION

Corresponding Authors

Haidong Zhou − *Department of Physics and Astronomy, University of Tennessee, Knoxville, Tennessee 37996, United States*; orcid.org/0000-0002-1595-1912; Email: hzhou10@utk.edu

Jie Ma − *Key Laboratory of Artificial Structures and Quantum Control, Shenyang National Laboratory for Materials Science, School of Physics and Astronomy, Shanghai Jiao Tong University, Shanghai 200240, China; Wuhan National High Magnetic Field Center, Huazhong University of Science and Technology, Wuhan 430070, China*; Email: jma3@sjtu.edu.cn

Authors

Jinlong Jiao − *Key Laboratory of Artificial Structures and Quantum Control, Shenyang National Laboratory for Materials Science, School of Physics and Astronomy, Shanghai Jiao Tong University, Shanghai 200240, China*; orcid.org/0000-0002-5896-3729

Shangshun Zhang − *School of Physics and Astronomy and William I. Fine Theoretical Physics Institute, University of Minnesota, Minneapolis, Minnesota 55455, United States*; orcid.org/0000-0001-8091-5224

Qing Huang − *Department of Physics and Astronomy, University of Tennessee, Knoxville, Tennessee 37996, United States*

M. Zhang − *Key Laboratory of Artificial Structures and Quantum Control, Shenyang National Laboratory for Materials Science, School of Physics and Astronomy, Shanghai Jiao Tong University, Shanghai 200240, China*

M.F. Shu − *Key Laboratory of Artificial Structures and Quantum Control, Shenyang National Laboratory for Materials Science, School of Physics and Astronomy, Shanghai Jiao Tong University, Shanghai 200240, China*

G. T. Lin − *Key Laboratory of Artificial Structures and Quantum Control, Shenyang National Laboratory for Materials Science, School of Physics and Astronomy, Shanghai Jiao Tong University, Shanghai 200240, China*

C. R. dela Cruz − *Neutron Scattering Division, Oak Ridge National Laboratory, Oak Ridge, Tennessee 37831, United States*

V. O. Garlea − *Neutron Scattering Division, Oak Ridge National Laboratory, Oak Ridge, Tennessee 37831, United States*

N. Butch − *Center for Neutron Research, National Institute of Standards and Technology, MS 6100 Gaithersburg, Maryland, United States*

M. Matsuda − *Neutron Scattering Division, Oak Ridge National Laboratory, Oak Ridge, Tennessee 37831, United States*

Complete contact information is available at: https://pubs.acs.org/10.1021/acs.chemmater.2c01576

Author Contributions

[+]J.J. and S.Z. contributed equally.

Notes

The authors declare no competing financial interest.

https://doi.org/10.1021/acs.chemmater.2c01576
Chem. Mater. 2022, 34, 6617−6625

■ ACKNOWLEDGMENTS

H.Z. and J.M. gratefully acknowledge the helpful discussions of Dr. Martin Mourigal, the Georgia Institute of Technology. J.J., M.Z., M.F.S., G.T.L., and J.M. thank the financial support from the National Science Foundation of China (Nos. U2032213, 11774223, and 12004243), the interdisciplinary program Wuhan National High Magnetic Field Center (Grant No. WHMFC 202122), Huazhong University of Science and Technology, and the National Key Research and Development Program of China (Grant No. 2018YFA0704300). G.T.L. thanks the project funded by China Postdoctoral Science Foundation (Grant No. 2019M661474). J.M. thanks a Shanghai talent program. Q.H. and H.Z. thank the support from NSF-DMR-2003117. The ND experiment was performed at HB-2A of HFIR, and INS experiments were performed at HYSPEC of SNS and DCS of NCNR. A portion of this research used resources at the High Flux Isotope Reactor and the Spallation Neutron Source, DOE Office of Science User Facilities operated by the Oak Ridge National Laboratory.

■ REFERENCES

(1) Balents, L. Spin liquids in frustrated magnets. *Nature* **2010**, *464*, 199−208.
(2) Moessner, R.; Ramirez, A. P. Geometrical frustration. *Phys. Today* **2006**, *59*, 24−29.
(3) Anderson, P. W. Resonating valence bonds: A new kind of insulator? *Mater. Res. Bull.* **1973**, *8*, 153−160.
(4) Fazekas, P.; Anderson, P. W. On the ground state properties of the anisotropic triangular antiferromagnet. *Philos. Mag.* **1974**, *30*, 423−440.
(5) Mezio, A.; Manuel, L. O.; Singh, R. R. P.; Trumper, A. E. Low temperature properties of the triangular-lattice antiferromagnet: a bosonic spinon theory. *New J. Phys.* **2012**, *14*, 123033.
(6) Mermin, N. D.; Wagner, H. Absence of Ferromagnetism or Antiferromagnetism in One- or Two-Dimensional Isotropic Heisenberg Models. *Phys. Rev. Lett.* **1966**, *17*, 1133−1136.
(7) Mourigal, M.; Fuhrman, W. T.; Chernyshev, A. L.; Zhitomirsky, M. E. Dynamical structure factor of the triangular-lattice antiferromagnet. *Phys. Rev. B* **2013**, *88*, No. 094407.
(8) Ma, J.; Kamiya, Y.; Hong, T.; Cao, H. B.; Ehlers, G.; Tian, W.; Batista, C. D.; Dun, Z. L.; Zhou, H. D.; Matsuda, M. Static and Dynamical Properties of the Spin-1/2 Equilateral Triangular-Lattice Antiferromagnet $Ba_3CoSb_2O_9$. *Phys. Rev. Lett.* **2016**, *116*, No. 087201.
(9) Ito, S.; Kurita, N.; Tanaka, H.; Ohira-Kawamura, S.; Nakajima, K.; Itoh, S.; Kuwahara, K.; Kakurai, K. Structure of the magnetic excitations in the spin-1/2 triangular-lattice Heisenberg antiferromagnet $Ba_3CoSb_2O_9$. *Nat. Commun.* **2017**, *8*, 235.
(10) Kamiya, Y.; Ge, L.; Hong, T.; Qiu, Y.; Quintero-Castro, D. L.; Lu, Z.; Cao, H. B.; Matsuda, M.; Choi, E. S.; Batista, C. D.; Mourigal, M.; Zhou, H. D.; Ma, J. The nature of spin excitations in the one-third magnetization plateau phase of $Ba_3CoSb_2O_9$. *Nat. Commun.* **2018**, *9*, 2666.
(11) Macdougal, D.; Williams, S.; Prabhakaran, D.; Bewley, R. I.; Voneshen, D. J.; Coldea, R. Avoided quasiparticle decay and enhanced excitation continuum in the spin-1/2 near-Heisenberg triangular antiferromagnet $Ba_3CoSb_2O_9$. *Phys. Rev. B* **2020**, *102*, No. 064421.
(12) Shirata, Y.; Tanaka, H.; Matsuo, A.; Kindo, K. Experimental realization of a spin-1/2 triangular-lattice Heisenberg antiferromagnet. *Phys. Rev. Lett.* **2012**, *108*, No. 057205.
(13) Zhou, H. D.; Xu, C.; Hallas, A. M.; Silverstein, H. J.; Wiebe, C. R.; Umegaki, I.; Yan, J. Q.; Murphy, T. P.; Park, J. H.; Qiu, Y.; Copley, J. R.; Gardner, J. S.; Takano, Y. Successive phase transitions and extended spin-excitation continuum in the S = 1/2 triangular-lattice antiferromagnet $Ba_3CoSb_2O_9$. *Phys. Rev. Lett.* **2012**, *109*, 267206.
(14) Susuki, T.; Kurita, N.; Tanaka, T.; Nojiri, H.; Matsuo, A.; Kindo, K.; Tanaka, H. Magnetization process and collective excitations in the S = 1/2 triangular-lattice Heisenberg antiferromagnet $Ba_3CoSb_2O_9$. *Phys. Rev. Lett.* **2013**, *110*, 267201.
(15) Fortune, N. A.; Huang, Q.; Hong, T.; Ma, J.; Choi, E. S.; Hannahs, S. T.; Zhao, Z. Y.; Sun, X. F.; Takano, Y.; Zhou, H. D. Evolution of magnetic field induced ordering in the layered quantum Heisenberg triangular-lattice antiferromagnet $Ba_3CoSb_2O_9$. *Phys. Rev. B* **2021**, *103*, 184425.
(16) Hwang, J.; Choi, E. S.; Ye, F.; Dela Cruz, C. R.; Xin, Y.; Zhou, H. D.; Schlottmann, P. Successive magnetic phase transitions and multiferroicity in the spin-one triangular-lattice antiferromagnet $Ba_3NiNb_2O_9$. *Phys. Rev. Lett.* **2012**, *109*, 257205.
(17) Lee, M.; Choi, E. S.; Huang, X.; Ma, J.; Dela Cruz, C. R.; Matsuda, M.; Tian, W.; Dun, Z. L.; Dong, S.; Zhou, H. D. Magnetic phase diagram and multiferroicity of$Ba_3MnNb_2O_9$: A spin-5/2 triangular lattice antiferromagnet with weak easy-axis anisotropy. *Phys. Rev. B* **2014**, *90*, 224402.
(18) Lee, M.; Hwang, J.; Choi, E. S.; Ma, J.; Dela Cruz, C. R.; Zhu, M.; Ke, X.; Dun, Z. L.; Zhou, H. D. Series of phase transitions and multiferroicity in the quasi-two-dimensional spin-1/2 triangular-lattice antiferromagnet $Ba_3CoNb_2O_9$. *Phys. Rev. B* **2014**, *89*, 104420.
(19) Lu, Z.; Ge, L.; Wang, G.; Russina, M.; Günther, G.; dela Cruz, C. R.; Sinclair, R.; Zhou, H. D.; Ma, J. Lattice distortion effects on the frustrated spin-1 triangular-antiferromagnet $A_3NiNb_2O_9$ (A = Ba, Sr, and Ca). *Phys. Rev. B* **2018**, *98*, No. 094412.
(20) Rawl, R.; Ge, L.; Agrawal, H.; Kamiya, Y.; Dela Cruz, C. R.; Butch, N. P.; Sun, X. F.; Lee, M.; Choi, E. S.; Oitmaa, J.; Batista, C. D.; Mourigal, M.; Zhou, H. D.; Ma, J. $Ba_8CoNb_6O_{24}$: A spin-1/2 triangular-lattice Heisenberg antiferromagnet in the 2D limit. *Phys. Rev. B* **2017**, *95*, No. 060412.
(21) Cui, Y.; Dai, J.; Zhou, P.; Wang, P. S.; Li, T. R.; Song, W. H.; Wang, J. C.; Ma, L.; Zhang, Z.; Li, S. Y.; Luke, G. M.; Normand, B.; Xiang, T.; Yu, W. Mermin-Wagner physics, (H,T) phase diagram, and candidate quantum spin-liquid phase in the spin-1/2 triangular-lattice antiferromagnet $Ba_8CoNb_6O_{24}$. *Phys. Rev. Materials* **2018**, *2*, No. 044403.
(22) Rawl, R.; Ge, L.; Lu, Z.; Evenson, Z.; Dela Cruz, C. R.; Huang, Q.; Lee, M.; Choi, E. S.; Mourigal, M.; Zhou, H. D.; Ma, J. $Ba_8MnNb_6O_{24}$: A model two-dimensional spin-5/2 triangular lattice antiferromagnet. *Phys. Rev. Materials* **2019**, *3*, No. 054412.
(23) Doi, Y.; Hinatsu, Y.; Ohoyama, K. Structural and magnetic properties of pseudo-two-dimensional triangular antiferromagnets $Ba_3MSb_2O_9$(M = Mn, Co, and Ni). *J. Phys.: Condens. Matter* **2004**, *16*, 8923−8935.
(24) Janson, O.; Tsirlin, A. A.; Sichelschmidt, J.; Skourski, Y.; Weickert, F.; Rosner, H. Long-range superexchange in $Cu_2A_2O_7$(A = P, As, V) as a key element of the microscopic magnetic model. *Phys. Rev. B* **2011**, *83*, No. 094435.
(25) Jiao, J. L.; Zhang, H. P.; Huang, Q.; Wang, W.; Sinclair, R.; Wang, G.; Ren, Q.; Lin, G. T.; Huq, A.; Zhou, H. D.; Li, M. Z.; Ma, J. Orbital competition of Mn^{3+} and V^{3+} ions in $Mn_{1+x}V_{2-x}O_4$. *J. Phys.: Condens. Matter* **2021**, DOI: 10.1088/1361-648X/abd9a1.
(26) Rodríguez-Carvajal, J. Recent advances in magnetic structure determination by neutron powder diffraction. *Phys. B: Condens. Matter* **1993**, *192*, 55−69.
(27) Shannon, R. D. Revised effective ionic radii and systematic studies of interatomic distances in halides and chalcogenides. *Acta Crystallogr. A* **1976**, *32*, 751−767.
(28) Zhang, Z.; Ma, X.; Li, J.; Wang, G.; Adroja, D. T.; Perring, T. P.; Liu, W.; Jin, F.; Ji, J.; Wang, Y.; Kamiya, Y.; Wang, X.; Ma, J.; Zhang, Q. Crystalline electric field excitations in the quantum spin liquid candidate $NaYbSe_2$. *Phys. Rev. B* **2021**, *103*, No. 035144.
(29) Liu, W.; Zhang, Z.; Ji, J.; Liu, Y.; Li, J.; Wang, X.; Lei, H.; Chen, G.; Zhang, Q. Rare-Earth Chalcogenides: A Large Family of Triangular Lattice Spin Liquid Candidates. *Chin. Phys. Lett.* **2018**, *35*, 117501.
(30) Baenitz, M.; Schlender, P.; Sichelschmidt, J.; Onykiienko, Y. A.; Zangeneh, Z.; Ranjith, K. M.; Sarkar, R.; Hozoi, L.; Walker, H. C.;

Orain, J. C.; Yasuoka, H.; van den Brink, J.; Klauss, H. H.; Inosov, D. S.; Doert, T. $NaYbS_2$: A planar spin-1/2 triangular-lattice magnet and putative spin liquid. *Phys. Rev. B* **2018**, *98*, 220409.
(31) Bordelon, M. M.; Kenney, E.; Liu, C.; Hogan, T.; Posthuma, L.; Kavand, M.; Lyu, Y.; Sherwin, M.; Butch, N. P.; Brown, C.; Graf, M. J.; Balents, L.; Wilson, S. D. Field-tunable quantum disordered ground state in the triangular-lattice antiferromagnet $NaYbO_2$. *Nat. Phys.* **2019**, *15*, 1058−1064.
(32) Kim, C.; Jeong, J.; Lin, G.; Park, P.; Masuda, T.; Asai, S.; Itoh, S.; Kim, H. S.; Zhou, H.; Ma, J.; Park, J. G. Antiferromagnetic Kitaev interaction in Jeff = 1/2 cobalt honeycomb materials $Na_3Co_2SbO_6$ and $Na_2Co_2TeO_6$. *J. Phys.: Condens. Matter* **2021**, *34*, No. 045802.
(33) Lin, G.; Jeong, J.; Kim, C.; Wang, Y.; Huang, Q.; Masuda, T.; Asai, S.; Itoh, S.; Gunther, G.; Russina, M.; Lu, Z.; Sheng, J.; Wang, L.; Wang, J.; Wang, G.; Ren, Q.; Xi, C.; Tong, W.; Ling, L.; Liu, Z.; Wu, L.; Mei, J.; Qu, Z.; Zhou, H.; Wang, X.; Park, J. G.; Wan, Y.; Ma, J. Field-induced quantum spin disordered state in spin-1/2 honeycomb magnet $Na_2Co_2TeO_6$. *Nat. Commun.* **2021**, *12*, 5559.
(34) Chernyshev, A. L.; Zhitomirsky, M. E. Spin waves in a triangular lattice antiferromagnet: Decays, spectrum renormalization, and singularities. *Phys. Rev. B* **2009**, *79*, 144416.
(35) Plumer, M. L.; Caille, A.; Hood, K. Multicritical points in the magnetic phase diagrams of axial and planar antiferromagnets. *Phys. Rev. B* **1989**, *39*, 4489−4499.
(36) B. Kleine, E. M.-H.; Frahm, K.; Fazekas, P. Spin-wave analysis of easy-axis quantum antiferromagnets on the triangular lattice. *Z. Phys. B Condens. Matter* **1992**, *87*, 103−110.
(37) Collins, M. F.; Petrenko, O. A. Triangular Antiferromagnets. *Can. J. Phys.* **1997**, *75*, 605−655.
(38) Luca Capriotti, A. E. T.; Sorella, Sandro Long-Range Néel Order in the Triangular Heisenberg Model. *Phys. Rev. Lett.* **1999**, *82*, 3989−3902.
(39) Chen, L.; Qu, D.-W.; Li, H.; Chen, B.-B.; Gong, S.-S.; von Delft, J.; Weichselbaum, A.; Li, W. Two-temperature scales in the triangular-lattice Heisenberg antiferromagnet. *Phys. Rev. B* **2019**, *99*, 140404.
(40) Yun, M.; Jeon, G. S. Classical Heisenberg antiferromagnet on a triangular lattice in the presence of single-ion anisotropy. *J. Phys.: Conf. Ser.* **2015**, *592*, No. 012111.
(41) Yokota, K.; Kurita, N.; Tanaka, H. Magnetic phase diagram of the S = 1/2 triangular-lattice Heisenberg antiferromagnet $Ba_3CoNb_2O_9$. *Phys. Rev. B* **2014**, *90*, No. 014403.
(42) Liu, H.; Khaliullin, G. Pseudospin exchange interactions in d^7 cobalt compounds: Possible realization of the Kitaev model. *Phys. Rev. B* **2018**, *97*, No. 014407.
(43) Chen, Q.; Verrier, A.; Ziat, D.; Clune, A. J.; Rouane, R.; Bazier-Matte, X.; Wang, G.; Calder, S.; Taddei, K. M.; Cruz, C. R. d.; Kolesnikov, A. I.; Ma, J.; Cheng, J. G.; Liu, Z.; Quilliam, J. A.; Musfeldt, J. L.; Zhou, H. D.; Aczel, A. A. Realization of the orbital-selective Mott state at the molecular level in $Ba_3LaRu_2O_9$. *Phys. Rev. Materials* **2020**, *4*, No. 064409.
(44) Zhou, J. S.; Goodenough, J. B. Intrinsic structural distortion in orthorhombic perovskite oxides. *Phys. Rev. B* **2008**, *77*, 132104.
(45) Nakayama, G.; Hara, S.; Sato, H.; Narumi, Y.; Nojiri, H. Synthesis and magnetic properties of a new series of triangular-lattice magnets, $Na_2BaMV_2O_8$ (M = Ni, Co, and Mn). *J. Phys.: Condens. Matter* **2013**, *25*, 116003.
(46) Rawl, R.; Lee, M.; Choi, E. S.; Li, G.; Chen, K. W.; Baumbach, R.; dela Cruz, C. R.; Ma, J.; Zhou, H. D. Magnetic properties of the triangular lattice magnets $A_4B'B_2O_{12}$ (A = Ba, Sr, La; B′=Co, Ni, Mn; B = W, Re). *Phys. Rev. B* **2017**, *95*, 174438.
(47) Azuah, R. T.; Kneller, L. R.; Qiu, Y.; Tregenna-Piggott, P. L.; Brown, C. M.; Copley, J. R.; Dimeo, R. M. DAVE: A Comprehensive Software Suite for the Reduction, Visualization, and Analysis of Low Energy Neutron Spectroscopic Data. *J. Res. Natl. Inst. Stand. Technol.* **2009**, *114*, 341−358.

https://doi.org/10.1021/acs.chemmater.2c01576
Chem. Mater. 2022, 34, 6617−6625